# Persistent Microporosity of a Non-planar Porphyrinoid based on Multiple Supramolecular Interactions for Nanomechanical Sensor Applications

| | |
|---|---|
| Journal: | *Materials Chemistry Frontiers* |
| Manuscript ID | QM-RES-10-2022-001039.R1 |
| Article Type: | Research Article |
| Date Submitted by the Author: | 30-Nov-2022 |
| Complete List of Authors: | Chahal, Mandeep K.; International Center for Materials Nanoarchitectonics National Institute for Materials Science<br>Maji, Subrata; Research Center for Functional Materials National Institute for Materials Science<br>Liyanage, Anuradha; University of North Texas<br>Matsushita, Yoshitaka; Research and Facilities Division National Institute for Materials Science<br>Hill, Pelin Jonathan; National Institute for Materials Science, International Center for Young Scientists<br>Payne, Daniel; International Center for Young Scientists National Institute for Materials Science<br>Jevasuwan, Wipakorn; International Center for Materials Nanoarchitectonics National Institute for Materials Science<br>Fukata, Naoki; International Center for Materials Nanoarchitectonics National Institute for Materials Science<br>Karr, Paul; Wayne State College<br>Labuta, Jan; International Center for Materials Nanoarchitectonics National Institute for Materials Science<br>Shrestha, Lok Kumar; International Center for Materials Nanoarchitectonics National Institute for Materials Science<br>Ishihara, Shinsuke; International Center for Materials Nanoarchitectonics National Institute for Materials Science<br>Ariga, Katsuhiko; International Center for Materials Nanoarchitectonics National Institute for Materials Science<br>D'Souza, Francis; University of North Texas<br>Yoshikawa, Genki; Research Center for Functional Materials National Institute for Materials Science<br>Yamauchi, Yusuke; International Center for Materials Nanoarchitectonics National Institute for Materials Science<br>Hill, Jonathan; International Center for Materials Nanoarchitectonics National Institute for Materials Science |
| | |

ARTICLE

# Persistent Microporosity of a Non-planar Porphyrinoid based on Multiple Supramolecular Interactions for Nanomechanical Sensor Applications[†]

Received 00th January 20xx,
Accepted 00th January 20xx

DOI: 10.1039/x0xx00000x

Mandeep K. Chahal[a], Subrata Maji[b], Anuradha Liyanage[c], Yoshitaka Matsushita[d], Pelin Tozman[e,f], Daniel T. Payne[a,e], Wipakorn Jevasuwan[a], Naoki Fukata[a], Paul A. Karr[g], Jan Labuta[a,h], Lok Kumar Shrestha[a,h], Shinsuke Ishihara,[a,h] Katsuhiko Ariga[a,h,i], Francis D'Souza[c], Genki Yoshikawa[b], Yusuke Yamauchi,[a,h,j] and Jonathan P. Hill[a,h]*

Porous substances such as metal-organic frameworks (MOFs), covalent organic frameworks (COFs) and zeolites are important materials for different applications, and several methods have been developed for their processing into device architectures. Solution processing of small molecule precursors into corresponding porous structures would be beneficial for many applications since it facilitates incorporation of the active material component into relevant devices thus reducing complexity and cost. Here we report that a non-planar saddle-shaped N-heterocycle-fused metallo-porphyrinoid forms a persistently microporous crystalline material directly from solution, which can undergo solvent exchange without loss of microporosity. The material is formed by a unique accumulation of intermolecular interactions involving π-π stacking of fused heterocycle, coordinative interactions at metalloporphyrinoid unit, and hydrogen bonding. This intermolecular multipoint interaction concept will be key in the future molecular design for on-demand synthesis of porous materials, and the simple implementation of the compound described here indicates the excellent potential for device materials' synthesis. Sensing properties of the material incorporated into a nanomechanical sensor array are also reported.

## Introduction

Supramolecular chemistry of porous materials is now a mature field with several well-defined types of material having become available over the past few decades including metal-organic-frameworks (MOFs),[1,2] porous coordination polymers (PCPs),[3] porous supramolecular assemblies[4] and even porous liquids.[5] The beauty of these substances lies not only in their highly aesthetically pleasing nanoarchitectures but also their great potential for real-world applications partly by analogy with purely inorganic porous materials such as zeolites[6] but also by the vast tunability of properties presented by combining organic and coordination chemistry synthetic methods.[7-10] With this in mind, it is an interesting challenge to introduce novelty to the mechanism of formation or components of porous materials especially where improvements in parameters such as processability or framework properties are required. This is partly because of the methods used to prepare, for instance, MOF materials where relatively harsh solvothermal conditions[‡] are often applied leading to products with excellent textural properties but usually poor handleability.

While advances in processing of MOF materials have been made,[11] there also exist a range of other structural motifs that have been introduced for the purpose of generating porosity in the resulting materials. Probably the best established of these so far are the hydrogen bonded organic frameworks (HOF's)[12] introduced by Wuest and coworkers.[13] An important forerunner of the HOFs can be found in Dianin's compound[14] whose structural properties are of substantial interest as a paradigm of host-guest complexation. Apart from HOFs, there are several other important classes of porous materials including porous organic cages,[15] which are generally obtained from cavity-containing molecules composing crystalline solids, as well as porous liquids,[16] where a porous molecular substance exhibits fluidity sufficient to be considered for certain applications. Each

---

[a] *International Center for Materials Nanoarchitectonics, National Institute for Materials Science, Namiki 1-1, Tsukuba, Ibaraki 305-0044, Japan. E_mail: jonathan.hill@nims.go.jp*
[b] *Olfactory Sensors Group, Research Center for Functional Materials, National Institute for Materials Science, Namiki 1-1, Tsukuba, Ibaraki 305-0044, Japan.*
[c] *Department of Chemistry, University of North Texas, 1155 Union Circle, 305070 Denton, Texas 76203, USA.*
[d] *Research Network and Facility Services Division, National Institute for Materials Science, 1-2-1 Sengen, Tsukuba, Ibaraki 305-0047, Japan.*
[e] *International Center for Young Scientists, National Institute for Materials Science, Namiki 1-1, Tsukuba, Ibaraki 305-0044, Japan.*
[f] *Magnetic Materials Analysis Group, Research Center for Magnetic and Spintronic Materials, National Institute for Materials Science, 1-2-1 Sengen, Tsukuba, Ibaraki 305-0047, Japan.*
[g] *Department of Physical Sciences and Mathematics, Wayne State College, 111 Main Street, Wayne, Nebraska, 68787, USA.*
[h] *JST-ERATO Yamauchi Materials Space-Tectonics Project, National Institute for Materials Science, Namiki 1-1, Tsukuba, Ibaraki 305-0044, Japan.*
[i] *Department of Advanced Materials Science, Graduate School of Frontier Sciences, The University of Tokyo, 5-1-5 Kashiwanoha, Kashiwa, Chiba 277-8561, Japan.*
[j] *Australian Institute for Bioengineering and Nanotechnology (AIBN), The University of Queensland, Brisbane, QLD 4072, Australia*

[†] Electronic Supplementary Information (ESI) available: [details of any supplementary information available should be included here]. See DOI: 10.1039/x0xx00000x

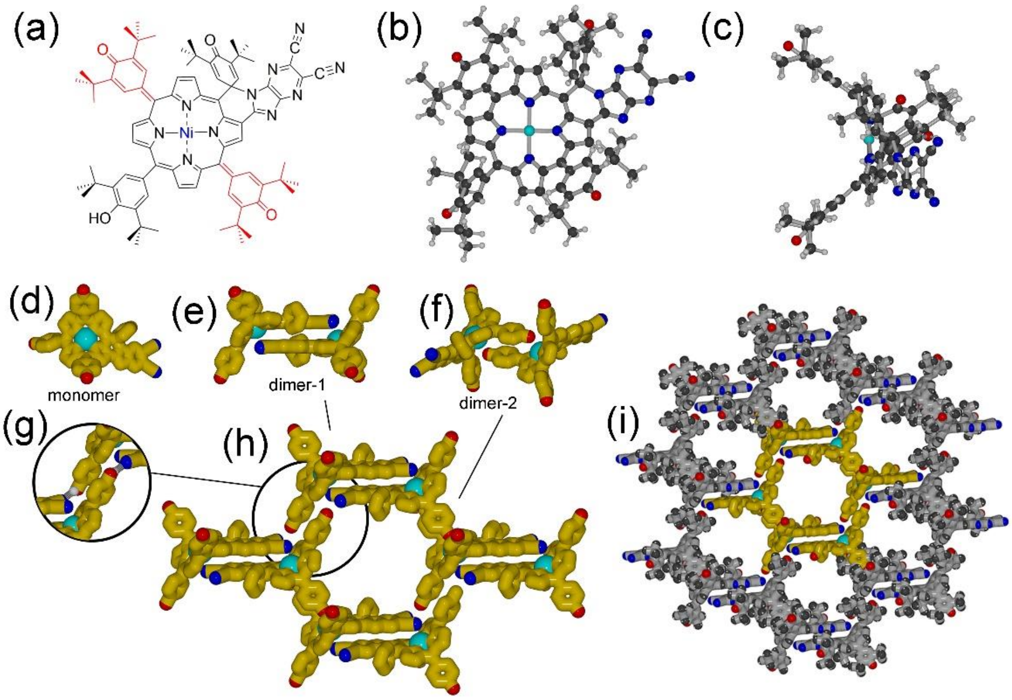

**Figure 1**. Chemical structure and simplified X-ray crystal structure of **1**-ox. (a) Chemical structure of **1**-ox. (b) Monomer with spiro-fused unit (Selected bond lengths: 1.888 Å ($N\text{-}Ni_{av}$), 1.2381(1) Å (C50-O2), 1.2332(1) Å (C18-O3)). (c) Edge-on view revealing the saddle geometry of **1**-ox. (d) Monomer unit: **1**-ox is presented as a yellow tecton with t-butyl groups removed and only structurally important heteroatoms shown in native colours (N: blue, O: red). Ni(II): light turquoise. (e) Dimer-1 unit formed by π-π stacking between the fused heterocyclic units (Interaction distances: 3.4674(1) Å (C64…N6: closest approach). (f) Dimer-2 unit formed from mutual C-O…Ni(II) coordinate bonds of the hemiquinonoid units (Interaction distances: 3.1205(1) Å (C-O...Ni(II)). (g) Hydrogen bonding coordination manifold formed at the encircled region (Interaction distances: 3.1572(1) Å (O1…N9)). (h) Formation of a pore structure by the dimer-1/2 units. (i) Hexagonal pore structure formed at longer range in the crystal (Pore dimensions: 6.8 Å × 11.68 Å). For ball-and-stick models of the analogous structures, see Figures S1–S9. See also CIF files in the Supplementary Information.

of the novel classes of porous material present particular advantages such as solution processability and large extrinsic surface areas.[17] Here we describe the synthesis and structure of a porous material that is complementary to these novel classes of compound in that it relies on a combination of intermolecular interactions including hydrogen bonding, π-π stacking and coordination interactions. The resulting porous crystalline material can be cast processed from solution and, in this case, has been applied as a sensing element in conjunction with membrane-type surface-stress sensors (MSS)[18,19] suggesting a possible application for this interesting class of compounds.

## Results and Discussion

### Structure.

Crystals of **1**-ox were grown by cooling hot solutions of the compound dissolved in toluene and the X-ray structure measured at 113 K is shown in Figure 1. The molecule is shown in stylized form due to the complexity of the interactions (details are given below; detailed structures in ball-and-stick format are shown in the Supporting Information (Figures S1–S9). The structure is composed according to two different dimer unit interactions with allied double mutual nitrile-phenol hydrogen bonding completing the system. The saddle-shaped **1**-ox molecule (Figure 1a-d) undergoes two different dimer interactions: dimer-1 (Figure 1e) is formed from mutual nitrile-Ni(II) coordinate bonds reinforced by π-π stacking between the planar electron deficient dinitrile-substituted fused heterocyclic units; dimer-2 (Figure 1f) is formed from mutual C-O…Ni(II) coordinate bonds involving hemiquinonoid meso-substituents. whose formation also depends on nitrile phenol H-bonding (Figure 1g). These dimer interactions lead to a pore structure (Figure 1h). The agglomeration of the intermolecular interactions results in the development of a bulk porous structure is shown in Figure 1i. In Figure 1, molecules depicted in yellow have some substituent groups removed for clarity; in Figure 1i, molecules shown in grey include all substituents illustrating that porosity is only slightly diminished by the presence of those groups. The importance of this structure lies in the fact that it forms directly from solution without the requirement for solvothermal treatment.

Crystals of coordination complexes grown using ambient solution techniques tend to lose structural integrity when removed from the mother liquors of their origin so that structural features such as pores are usually lost. In the case of **1**-ox, we were surprised to find that porosity is maintained even after removal of toluene contained in the structure by drying under reduced pressure at 120 °C for 24 h. Textural properties of **1**-ox following such treatment were determined using $N_2$ adsorption measurements and the data are shown in Figure 2a,b. Important parameters derived from these data are shown in Table 1. Figure 2c shows toluene encapsulated in a pore of **1**-ox viewed along the crystal a-axis. Three moles of toluene are

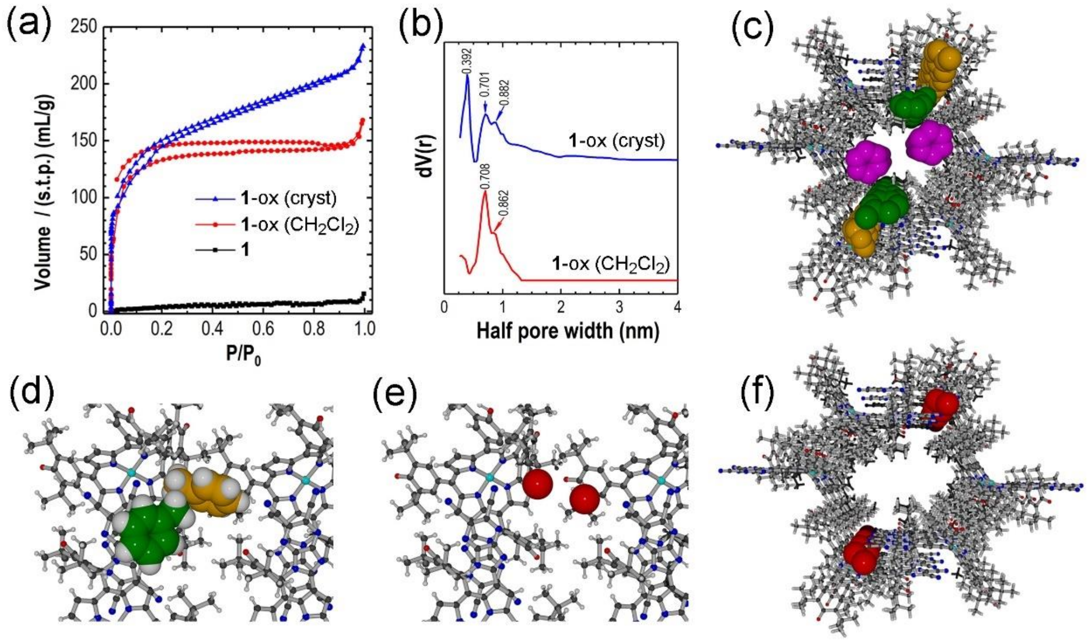

**Figure 2**. Porosity and solvent exchange of **1**-ox in crystalline and 'as-isolated' states. (a) Nitrogen adsorption isotherms of **1**, **1**-ox ($CH_2Cl_2$) (as isolated by column chromatography) and **1**-ox (cryst) (crystals grow by allowing a solution of **1**-ox in hot toluene to cool to r.t.). (b) Half pore widths obtained using DFT methods. **1**-ox (cryst) has a double pore architecture while **1**-ox ($CH_2Cl_2$) lacks porosity at 0.39 nm (see text). (c) Locations of encapsulated toluene molecules in a pore of **1**-ox (cryst) viewed along the *a*-axis (see also Figure S10). Three crystallographically unique locations are denoted in pink (pore centre, highly disordered, no pore wall contacts), green (adsorbed by π-π stacking at electron deficient fused imidazopyrazine-[2,3]-dicarbonitrile unit) and yellow (buried in pore wall, C-H…N≡C, and C-H…π interactions). (d) Detail of location of adsorbed toluene. (e) Water binding sites in adventitiously solvent-exchanged **1**-ox (cryst). $H_2O$ is disordered but proximity suggests mutual H-bonding and H-bonding with nitrile N atoms as well as lone pair-π interactions. (f) Location of $H_2O$ in pores coincides with that of the uniquely bound 'yellow' toluene in the pore wall. For more details see Figures S7, S8, S10 and CIF files in the Supplementary Information.

bound per unit cell each at a unique site, (i) in the pore void space (pink shading), (ii) adsorbed by π-π stacking at the electron deficient fused imidazopyrazine-[2,3]-dicarbonitrile unit (green, see also Figure 2d) and (iii) buried in the pore wall, C-H…N≡C, and C-H…π interactions (yellow, see also Figure 2d).

During X-ray crystallographic measurements, we noted that toluene solvent molecules were present in the structure at different stoichiometries (initially 2–3 eq. gradually reducing) suggesting that toluene can be evacuated from the pores as suggested by a large measured surface area of 475 $m^2\ g^{-1}$ (Table 1) for the crystals. In fact, when solvent was allowed to evaporate from samples of crystals stored in mineral oil, crystal integrity was maintained and, on cooling a crystal to a temperature suitable for single crystal X-ray diffraction the same structure was found then to accommodate 2 moles of $H_2O$ per unit cell (Figure 2e,f). Notably, these replace the toluene (yellow) molecule at the pore wall binding site. Furthermore, as-isolated samples of **1**-ox obtained by evaporation of its solutions in dichloromethane also exhibit large surface areas (SSA ~340 $m^2\ g^{-1}$, Table 1) suggesting that solvation by toluene is not a prerequisite to establish the porous structure of **1**-ox. Interestingly, **1**-ox ($CH_2Cl_2$) not only has a lower surface area but also lacks the smallest (0.392 nm half width, see Figure 2b) pore apparent in **1**-ox (cryst) probably indicating that selected binding sites of **1**-ox ($CH_2Cl_2$) are occupied (or absent). Thermogravimetric analyses on samples of the toluene solvate of **1**-ox prior to and following drying in air are shown in Figure S11. These data show a weight loss of 6.1 % wt. starting at 60 °C and complete by 150 °C assigned to the loss of solvent. The expected weight loss for two equivalents of toluene is 11.7 % suggesting that toluene is indeed rapidly lost from crystals of **1**-ox even under ambient conditions. While we can ascertain from X-ray crystal structure data that **1**-ox has three possible binding sites for toluene (see Figure 2c, Figure S10), it seems that solvent is lost rapidly directly following isolation of the crystals from the mother liquor especially from the central pore site

**Table 1.** Porosity properties obtained by DFT and BJH methods.

| Sample | *SSA* ($m^2\ g^{-1}$) | $S_{micro}$ ($m^2\ g^{-1}$) | $S_{meso}$ ($m^2\ g^{-1}$) | $V_p$ ($cm^3\ g^{-1}$) | $V_{micro}$ ($cm^3\ g^{-1}$) | $D_w$ (nm) | $D_p$ (nm) |
|---|---|---|---|---|---|---|---|
| **1** | 15.11 | 6.44 | 8.67 | 0.040 | 0.014 | 1.265 | 4.10 |
| **1**-ox ($CH_2Cl_2$) | 343.56 | 338.65 | 4.91 | 0.039 | 0.210 | 0.704 | 3.87 |
| **1**-ox (cryst) | 474.6 | 398.01 | 76.62 | 0.450 | 0.310 | 0.392 | 3.09 |

*SSA* = specific surface area, $S_{micro}$ = micropore surface area, $S_{meso}$ =mesopore surface area, $V_p$ = total pore volume, $V_{micro}$ = micropore volume, $D_w$ = half pore width, and $D_p$ = average mesopore diameter.

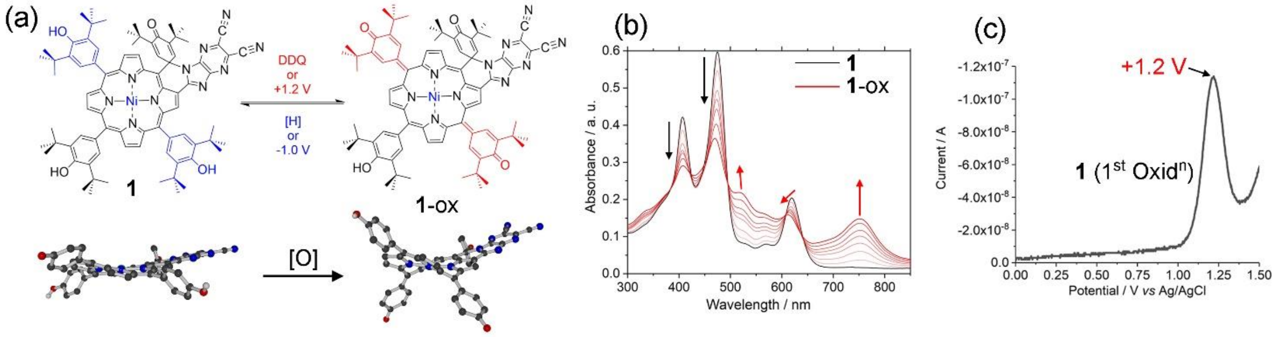

**Figure 3**. Formation of **1**-ox. (a) Chemical structures of **1** and **1**-ox, and methods/conditions for their interconversion, and change in molecular conformation on oxidation of **1** to **1**-ox. ([H] denotes reduction; for back reduction of **1**-ox during UV-vis monitoring with potential maintained at –0.4 V, see also Figure S14), and variation in molecular conformation from ruffled to a highly-puckered saddle structure. Red arrow in the lower plan views of the structures denotes the viewing direction of the upper side elevations. (b) Spectroelectrochemical measurements on **1** in 1,2-dichlorobenzene with solution maintained at +1.2 V. Note the emerging NIR electronic absorption at 753 nm assigned to increased conjugation between the relevant meso-substituents and the macrocycle. (c) Differential pulsed voltammogram of **1** in 1,2-dichlorobenzene showing the first 2-electron oxidation peak to **1**-ox.

(pink in Figure 2c), where toluene molecules have no specific binding modes and are highly disordered (Cif). Also, based on the relative weight loss in TGA and large disorder in toluene molecules bound through π-π stacking at the electron deficient fused imidazopyrazine-[2,3]-dicarbonitrile unit of **1**-ox (highlighted in green in Figure 2c), toluene molecules are subsequently lost preferentially from that site. Toluene molecules bound deeper in the pore wall appear to be adsorbed until crystals are subjected to higher temperature, which is consistent with the weight loss observed by TGA. Note that specific surface area determinations were performed after annealing of the samples at 120 °C under a nitrogen atmosphere leading to complete elimination of toluene from the samples prior to measurement. Polar solvent *N,N*-dimethylformamide (DMF) could also be used as a solvent with porosity of drop-cast samples having similar metrics (SSA ~250 $m^2\ g^{-1}$, see Figure S12a,b) to samples obtained by recrystallization from non-polar solvents toluene or dichloromethane (see Table 1). Material crystallized from DMF while also exhibiting stable porosity exhibits a different pXRD pattern suggesting a different bulk structure (see Figure S13) and solvatomorphism of **1**-ox. Finally, we have confirmed the long-term (12 months) porosity of a sample of **1**-ox (currently under investigation) prepared by recrystallization followed by storage in air under ambient conditions (in a glass vial; see Figure S12b,c). A high specific surface area (~780 $m^2\ g^{-1}$) with micro/mesoporosity was measured consistent with the initially prepared materials, although it is noted that the mesopore/micropore ratio is larger in the stored sample (from ~0.2 to ~0.4).

### Molecular Properties.

The non-planar conformation of **1**-ox is important for its assembly properties because of its saddle-like conformation and the availability of the opposing non-protonated (i.e., carbonyl) oxygen atoms for coordinative interactions with the Ni(II) center. Saddle conformations of porphyrin macrocycles have emerged during our investigations of the chemical synthetic properties of the porphyrin meso-tetrakis(3,5-di-t-butyl-4-hydroxyphenyl)porphyrin (TDtBHPP).[20,21,22] Previously, we have discovered a unique molecule having two peripheral substituents of the porphyrin connected through a spiro-type linkage[§] (containing a single quaternary carbon atom that links two otherwise independent heterocycles). An intramolecular process[23] leads to the reaction between adjacent substituents and fusion forming a spiro motif resulting in the molecule **1** – the precursor of **1**-ox in the present work (see Scheme S1 for the synthesis). Compound **1** remains prone to oxidation and can be converted to **1**-ox by further oxidation using DDQ accompanied by a new absorption band in the near infrared region at 753 nm (Figure 3b) which also emerges during spectroelectrochemical measurements on solutions of **1** held under a potential of 1.2 V (its first oxidation – see the differential pulsed voltammogram (DPV), Figure 3c). Figure 3a also shows a comparison of the X-ray crystal structures of **1** and **1**-ox revealing that oxidation is accompanied by a substantial change in structure from slightly ruffled (**1**) to a saddle-like form (**1**-ox).[24]

The importance of intermolecular interactions for the persistent porosity of **1**-ox is emphasized by the structure of compound **2**. This molecule is the result of nucleophilic substitution by hydroxide on **1**-ox in the presence of tetra-n-butylammonium fluoride (TBAF), i.e., under basic conditions, phenol moieties are known to be deprotonated.[25] In **2**, the spiro-linked quinonoid group is transferred fully to the *sp*$^3$ N atom of the benzimidazole substituent. A plausible mechanism for this process is shown in Figure S15 and the X-ray crystal structure of **2** is shown in Figure 4a,b. The synthesis of **2** from **1**-ox is accompanied by elimination of the π-π stacking unit caused by the substituent transfer and breaking of the spiro linkage, insertion of an oxo substituent at the porphyrin periphery, and inversion of the saddle conformation. There is the additional effect that hemiquinonoid substituents (shown in red in Figure 4) that in **1**-ox form strong mutual coordinate interactions with Ni(II) are now present as phenols capable only of hindered H-bonding. Thus, as shown in Figure 4b, only relatively weak OH…N (phenol-benzimidazole) and CN…H-C (nitrile-pyrrole) hydrogen bonding interactions remain for **2** leading to poor stability of its crystals and no persistent porosity (Surface area (**2**) = 21.2 $m^2\ g^{-1}$; see Figure S16 for surface area analysis of **2**).

While the introduction of macrocyclic saddle or curved conformations of tetrapyrroles[26] has sometimes been found to lead to porous structures,[27,28] these are generally not persistent and have also not been so far observed for the saddle-shaped 'quinophyrin' systems[24] most closely analogous with **1**-ox. Saddling of the macrocycle ought to improve the prospects for the formation of structural vacancies but **1**-ox is subject to multiple interactions in the structure. Not least of these is the face-to-face π-π stacking dimerization which establishes a doubly concave 'secondary building unit' (SBU) (Figure 1e). It is then important in this case to consider the availability of interdimer interactions of the SBU especially involving electronegative atoms that might coordinate to the Ni(II) cation. In **1**-ox, these are provided by substituent oxygen atoms, which undergo coordination to the Ni(II) cation of the metalloporphyrin unit (i.e. are not precluded by the bulky t-butyl substituents often associated with obstruction of such interactions). Overall, **1**-ox forms its stable porous network form through the culmination of the mutual intermolecular effects of π-π stacking, Ni(II)-carbonyl coordinative dimerization, with support of the structure by an allied OH…nitrile hydrogen bonding manifold and other C-H…X interactions. It illustrates the benefits of multipoint cooperativity to establish stable porous structures in supramolecular solvent-processable systems, which is also highlighted by the structure of **2** where many of the salient intermolecular features are eliminated leading to non-persistence of structure.

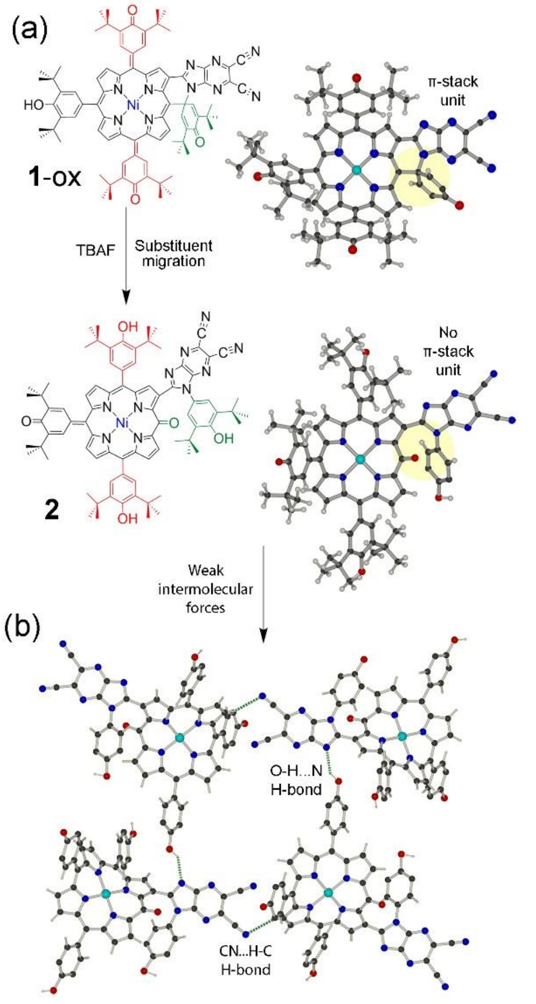

**Figure 4**. Substituent migration in **1**-ox and X-ray crystal structure of **2**. (a) Transformation of **1**-ox to **2** in the presence of tetra-n-butylammonium fluoride (left), and changes in the molecular structure: spiro substituent migration (centre) eliminates the π-stacking unit, and is accompanied by saddle inversion of conformation. Spiro substituent tBu groups removed for clarity. (b) X-ray crystal structure of **2** shows general paucity of strong intermolecular interactions (main hydrogen bonds shown) Important distances: O-H…N H-bond, O2-N10 (2.9613(83) Å); C≡N…H-C N8-H48 (2.5327(125) Å); N1-Ni (1.8985(65) Å); N2-Ni (1.8743(56) Å); N3-Ni (1.8986(55) Å), N4-Ni (1.8927(63) Å).

## Supramolecular Porous Receptor Layer

Since **1**-ox presents a persistently porous structure when processed from solution and this feature might promote sensing activity in the corresponding sensor devices, we have applied this material as a receptor layer for applications in strain-induced micro-electro-mechanical system (MEMS) sensors for multicomponent gas/vapor detection (also referred to as MSS[18,19,29]). Many of the materials used for this purpose are intractable porous monoliths or powders and are difficult to prepare as homogeneous dispersions, a feature required for the processing of the materials into an appropriate receptor film form for MSS applications. Furthermore, films formed from solvent dispersions of microparticulate materials are intrinsically unsuitable for this purpose since adhesion of the receptor layer to the MSS sensor is not sufficient to promote the strong coupling between receptor material and MEMS interface required for an effective sensing response. In this regard, the microporous structure of **1**-ox with solvent exchange characteristics and easy solution processability makes it an excellent choice for incorporation as the strain-induced sensor receptor layer. Deposition of the receptor layer from solution allows the formation of a polycrystalline film which is intimately bound at the MSS sensor interface resulting in strong coupling and a corresponding mechanical response in the presence of the analyte of interest, in this case vapor phase organic solvents or other volatile molecular species.

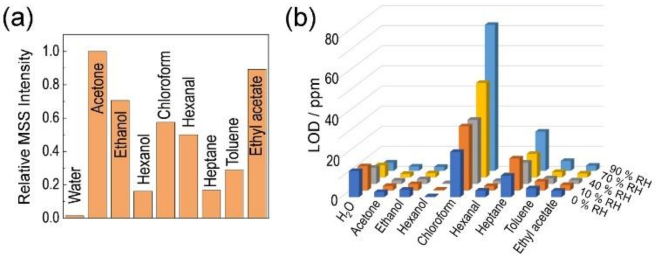

**Figure 5**. **1**-ox@MSS relative responses and limits of detection (LOD) under standard conditions. (a) Histogram of signal intensity for the VOCs relative to acetone (set to unity). (b) LOD of **1**-ox@MSS sensor for different VOCs at the different humidity levels.

The highly sensitive MSS platform with **1**-ox receptor layer (**1**-ox@MSS; Figure 5) although exhibiting lower selectivity under normal conditions (Figure 5a), shows good limits of detection (LOD) under conditions of high relative humidity (R.H.) (Figure 5b). **1**-ox@MSS also exhibits rapid and intense sensing signals for different VOCs (see Figure 6a). A significant feature is the extremely low sensitivity of **1**-ox@MSS towards water vapour (Figure 5a). This allows **1**-ox@MSS to be used for the detection of solvents under conditions of high humidity (Figure 6b). In particular, acetone vapour can be detected with optimum signal output enhanced over the other test solvents even at R.H. up to 90 %, making **1**-ox@MSS an excellent candidate for this purpose (Figure 6c). LOD for acetone at R.H. = 90 % based on comparison with data from the same samples obtained by proton transfer reaction mass spectrometry (PTR-MS, a standard method often used for breathanalysis) is around 2 ppm. Note that compounds with low porosity (such as the precursor **1**) lead to substantially weaker responses at the MSS sensor (e.g., see Figure S17; **1** exhibits an MSS response to acetone under the same conditions approx. 20% that of **1**-ox; 2 mV vs. 10 mV). While the material properties of **1**-ox are far superior to **1** for this application, it should be pointed out that there are several factors affecting the preparation of the sensing devices. The first of these is solvatomorphism since the use of each solvent (toluene, dichloromethane and N,N-dimethylformamide) to generate solid samples of **1**-ox apparently leads to different morphologies of solid although these are all microporous crystalline solids. Other factors include the quality of film formed by **1**-ox depending on solvent and the physical structures of analyte binding site formed on deposition from each solvent. The elucidation of these factors will be useful in the design of future molecular elements for application in conjunction with the MSS sensing device platform. In particular, given the wide library of compounds available, either porphyrinoids, porous materials, or both, there is excellent potential to identify highly effective sensors and sensor arrays based on informed design of the different materials. We do note here however that, of all the compounds tested to date, **1**-ox is the first molecular material to reach standards of sensitivity suitable for any applications prepared by our scalable ink-jet printing method.

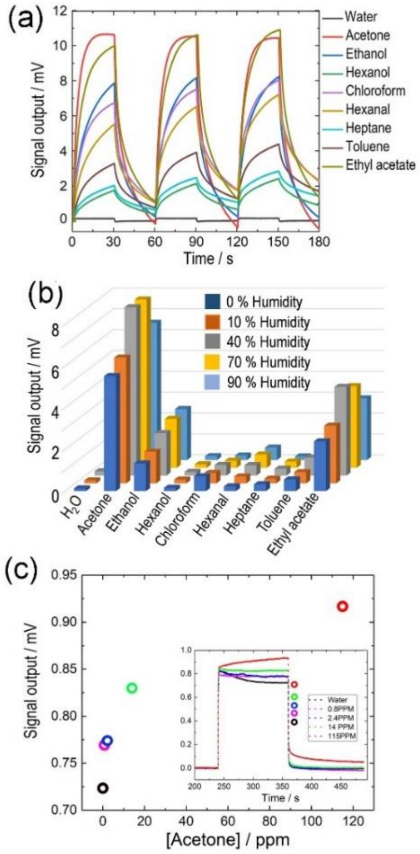

**Figure 6**. Sensing responses of **1**-ox@MSS to different vapors at room temperature (25 °C). (a) Output voltages of the **1**-ox@MSS device under the different VOCs at 20 % v/v. Composition: solvent saturated nitrogen stream (20%) mixed with pristine dry nitrogen (80%). Note that signal build-up occurs where the response of the film does not return to zero as analyte accumulates in the film. (b) Humidity dependence of sensor signals for different VOCs at 10 % v/v (solvent saturated nitrogen stream (10% by volume) mixed with nitrogen of different relative humidity (90% by volume) measured under five relative humidity conditions (RH = 0 – 90%). (c) **1**-ox@MSS sensor response to acetone plotted against actual acetone concentration measured using PTR-MS. LOD is around 2 ppm in humid air. Inset: **1**-ox@MSS sensor response to acetone at the limit of detection in humid air (RH 90%).

The availability of solution processable microporous receptor layers, such as **1**-ox, sensitive towards different biomarker molecules (e.g., acetone is a marker of certain disease states in mammals[30-32]) is critical for real-time applications in biomedical diagnosis or for quality control of foodstuffs, and complements existing chemical sensor technologies.[33-35] Regarding the practicality of acetone sensing using **1**-ox@MSS, based on the potential sub-ppm sensitivity under conditions of high humidity, this device is highly suitable for screening patients for disease states involving higher levels of acetone in breath samples. The low cost and simplicity of operation of such a device implies its application in remote field locations or in the offices of clinical practitioners. Normal breath acetone levels lie in the 0.5–2.0 ppm range.[30] Therefore, any disease state resulting in higher levels of breath acetone should be detectable using **1**-ox@MSS. Higher breath acetone levels can be found in patients with diabetes mellitus related to errors in carbohydrate metabolism.[36] For a similar reason, patients who are obese or starving also present with higher than normal acetone levels. Other states having the same symptom include lung cancer, congenital acidemia, and some infections making acetone useful as a diagnostic marker.[36] Finally, home monitoring of acetone in the breath could be used by individuals who are attempting to maintain ketogenic diets for purposes of weight loss.

## Conclusions

In summary, we report the remarkable self-assembly of saddle-shaped porphyrinoid **1**-ox into a microporous crystalline solid with excellent porosity by simple recrystallization processes or by a simple solution casting process. In the porous structure, sites for solvent adsorption are provided by hydrogen bonding, π-π stacking interactions, and condensation of solvent at the interior of the tubular voids in the remaining structure. The multipoint nature of the interactions to establish the persistently porous structure has been emphasized by considering a similarly structured molecule, **2** – a derivative of **1**-ox, whose form does not support the various required interactions. The properties of **1**-ox, and its receptor layer deposited from different solvents, suggest applications in solvent adsorption and sensing. For the latter, we have shown the enhanced sensitivity of **1**-ox in the solid state for the detection of gaseous analytes using the MSS nanomechanical sensor system. **1**-ox@MSS devices exhibit practically useful sensitivity towards different solvents even under conditions of high humidity making it suitable for real time monitoring of volatile analytes in, for example, human breath. Other examples in this series based on derivatives of **1**-ox will be reported in due course to further demonstrate the practical application of supramolecular materials.

## Data Availability

X-ray crystal structure data of the different solvates of **1**-ox, and **2** are supplied as CIF files. $^{1}$H & $^{13}$C NMR spectra, high-resolution mass spectra and electronic absorption spectra of the compounds are provided in the Supplementary Information (Figures S18-S37). Crystallographic data (excluding structure factors) have been deposited with the Cambridge Crystallographic Data Centre with CCDC reference numbers 2107801, 2107802, 2107803, 2107804 and 2209423. The CIF of the higher toluene solvate is also supplied here as Supplementary Information. Copies of the data can be obtained, free of charge, on application to CCDC, 12 Union Road, Cambridge CB2 1EZ, UK http://www.ccdc.cam.ac.uk/perl/catreq/catreq.cgi, e-mail: data_request@ ccdc.cam.ac.uk, or fax: +44 1223 336033.

## Author Contributions

M.K.C. designed and initiated the project, synthesized and characterized the molecules. S.M. and G.Y. analyzed the sensing properties of the molecules. A.L. and F.D. performed electrochemical and spectroelectrochemical analyses on solutions of the molecules. Y.M. performed single crystal X-ray crystallographic and powder X-ray diffraction experiments and refined the crystal structure data. P.T. and H.S-A. undertook magnetic measurements. D.T.P. J.W., and N.F. collected ESR spectra of the compounds. P.A.K. performed computational analysis of the molecules. J.L. modelled data sets. L.K.S., S.I., K.A. and Y.Y. examined the textural parameters of the materials. J.P.H. supervised the research, proposed and established the molecular design, and wrote the manuscript. All authors contributed to the final data analysis and preparation, and the writing and composition of the manuscript.

## Conflicts of interest

There are no conflicts to declare.

## Acknowledgements

The authors are grateful to Ms. Sabina Shahi (Central Dept. Chemistry, Tribhuvan University, Kirtipur, Kathmandu, Nepal) for performing thermogravimetry measurements. This work was partly supported by World Premier International Research Center Initiative (WPI Initiative), MEXT, Japan. This study was also supported by JSPS KAKEN-HI Grant Numbers JP19H05819 and JP19K05229. The authors are also grateful to JST-ERATO Yamauchi Materials Space-Tectonics Project (JPMJER2003) and the Queensland Node of the Australian National Fabrication Facility (ANFF-Q) for support.

## Notes and references

[‡] Solvothermal syntheses generally involve heating of precursors at elevated temperatures in aqueous (hydrothermal) or organic solvents or their mixtures in a PTFE-lined stainless-steel autoclave.

[§] Spiro-linkages, where a single atom is shared between at least two molecular rings, have the effect of preventing mutual rotation of the substituents. In this case, it leads to fusion of the electron deficient imidazo[4,5-b]pyrazine-5,6-dicarbonitrile with the electron rich porphyrin unit.

1 H. Furukawa, K. E. Cordova, M. O'Keeffe and O. M. Yaghi, The chemistry and applications of metal-organic frameworks, *Science*, 2013, **341**, 1230444.
2 S. Dang, Q.-L. Zhu and Q. Xu, Nanomaterials derived from metal-organic frameworks, *Nat. Rev. Mater.*, 2018, **3**, 17045.
3 S. Kitagawa, R. Kitaura and S. Noro, Functional porous coordination polymers, *Angew. Chem. Int. Ed.,* 2004, **43**, 2334.
4 A. Chaix, G. Mouchaham, A. Shkurenko, P. Hoang, B. Moosa, P. M. Bhatt, K. Adil, K. N. Salama, M. Eddaoudi and N. M. Khashab, Trianglamine-Based supramolecular organic framework with permanent intrinsic porosity and tunable selectivity, *J. Am. Chem. Soc.* 2018, **140**, 14571.
5 S. L. James, The dam bursts for porous liquids, *Adv. Mater.*, 2016, **28**, 5712.
6 J. Li, A. Corma and J. Yu, Synthesis of new zeolites, *Chem. Soc. Rev*., 2015, **44**, 7112.
7 D. Zhao, D. J. Timmons, D. Yuan and H.-C. Zhou, Tuning the topology and functionality of metal-organic frameworks by ligand design, *Acc. Chem. Res*., 2011, **44**, 123.
8 R.-R. Liang, S.-Y. Jiang, R.-H. A and X. Zhao, Two-dimensional covalent organic frameworks with hierarchical porosity, *Chem. Soc. Rev*., 2020, **49**, 3920.
9 M. S. Lohse and T. Bein, Covalent organic frameworks: structures, synthesis and applications, *Adv. Funct. Mater*., 2018, **28**, 1705553.
10 A. G. Slater and A. I. Cooper, Porous materials. Function-led design of new porous materials, *Science*, 2015, **348**, 988.
11 U.-J. Ryu, S. Jee, P. C. Rao, J. Shin, C. Ko, M. Yoon, K. S. Park and K. M. Choi, Recent advances in process engineering and upcoming applications of metal organic frameworks, *Coord. Chem. Rev.*, 2021, **426**, 213544.
12 X. Song, Y. Wang, C. Wang, D. Wang, G. Zhuang, K. O. Kirlikovali, P. Li, O. M. Farha, Design rules of hydrogen-bonded organic frameworks with high chemical and thermal stabilities, *J. Am. Chem. Soc.*, 2022, **144**, 10663–10687.
13 P. Brunet, M. Simard, J. D. Wuest, Molecular tectonics. Porous hydrogen-bonded networks with unprecedented structural integrity, *J. Am. Chem. Soc.*, 1997, **119**, 2737–2738.
14 G. O. Lloyd, M. W. Bredenkamp, L. J. Barbour, Enclathration of morpholinium cations by Dianin's compound: salt formation by partial host-to-guest proton transfer, *Chem. Commun.*, 2005, 4053–4055, and references cited therein.
15 M. A. Little, A. I. Cooper, The chemistry of porous organic materials, *Adv. Funct. Mater.*, 2020, **30**, 1909842.
16 A. I. Cooper, Porous molecular solids, *ACS Cent. Sci.*, 2017, **3**, 544–553.

17 T. D. Bennett, F.-X. Coudert, S. L. James, A. I. Cooper, The changing state of porous materials, *Nat. Mater.*, 2021, **20**, 1179 – 1187.

18 G. Yoshikawa, T. Akiyama, S. Gautsch, P. Vettiger, H. Rohrer, Nanomechanical membrane-type surface stress sensor, *Nano Lett.*, 2011, **11**, 1044

19 H. H.-M.Yeung, G. Yoshikawa, K. Minami and K. Shiba, Strain-based chemical sensing using metal-organic framework nanoparticles, *J. Mater. Chem. A*, 2020, **8**, 18007.

20 M. K. Chahal, A. Liyanage, H. B. Gobeze, D. T. Payne, K. Ariga, J. P.Hill and F. D'Souza, Supramolecular ultrafast energy and electron transfer in a directly Linked BODIPY-oxoporphyrinogen dyad upon fluoride ion binding, *Chem. Commun.*, 2020, **56**, 3855.

21 M. K. Chahal, J. Labuta, V. Březina, P. A. Karr, Y. Matsushita, W. A. Webre, D. T. Payne, K. Ariga, F. D'Souza and J. P. Hill, Knock-on synthesis of tritopic calix[4]pyrrole host for enhanced anion interactions, *Dalton Trans.*, 2019, **48**, 15583.

22 M. K. Chahal, A. Liyanage, A. Z. Alsaleh, P. A. Karr, J. P. Hill and F. D'Souza, Anion-enhanced excited state charge separation in a spiro-locked N-heterocycle-fused push-pull zinc porphyrin, *Chem. Sci*., 2021, **12**, 4925.

23 H. Yamashita, T. Ikezawa, Y. Kobayashi and J. Abe, J. Photochromic phenoxyl-imidazolyl radical complexes with decoloration rates from tens of nanoseconds to seconds, *J. Am. Chem. Soc*., 2015, **137**, 4952.

24 S. Ishihara, J. P. Hill, A. Shundo, K. Ohkubo, S. Fukuzumi, M. R. J. Elsegood, S. J. Teat and K. Ariga, Reversible Photoredox Switching of Porphyrin-bridged Bis-2,6-di-*t*-Butyl Phenols, *J. Am. Chem. Soc.*, 2011, **133**, 16119.

25 A. Shundo, J. P. Hill, K. Ariga, Toward volatile and non-volatile molecular memories: fluorescence switching based on fluoride-triggered interconversion of simple porphyrin derivatives, *Chem. Eur. J.*, 2009, **15**, 2486.

26 T. Ishizuka, N. Grover, C. J. Kingsbury, H. Kotani, M. O. Senge and T. Kojima, Nonplanar porphyrins: synthesis, properties, and unique functionalities, *Chem. Soc. Rev.*, 2022, **51**, 7560.

27 T. Ishizuka, M. Sankar, Y. Yamada, S. Fukuzumi and T. Kojima, Porphyrin nanochannels reinforced by hydrogen bonding, *Chem. Commun*., 2012, **48**, 6481.

28 M. J. Smith, W. Clegg, K. A. Nguyen, J. E. Rogers, R. Pachter, P. A. Fleitz and H. L. Anderson, Synthesis and crystal structure of a push-pull quinoidal porphyrin: a nanoporous framework assembled from cyclic trimer aggregates, *Chem. Commun*., 2005, **41**, 2433.

29 G. Yoshikawa, T. Akiyama, F. Loizeau, K. Shiba, S. Gautsch, T. Nakayama, P. Vettiger, N. F. de Rooij and M. Aono, Two-dimensional array of piezoresistive nanomechanical membrane-type surface stress sensor (MSS) with improved sensitivity, *Sensors*, 2012, **12**, 15873.

30 J. C. Anderson, Measuring breath acetone for monitoring fat loss: review, *Obesity*, 2015, **23**, 2327.

31 D. Hill and R. Binions, Breath Analysis for Medical Diagnosis, *Int. J. Smart Sensing Intell. Syst*., 2012, **5**, 401.

32 Z. Wang and C. Wang, Is breath acetone a biomarker of diabetes? A historical review on breath acetone measurements, *J Breath Res.*, 2013, **7**, 037109.

33 R. Paolesse, S. Nardis, D. Monti, M. Stefanelli and C. Di Natale, Porphyrinoids for Chemical Sensor Applications, *Chem. Rev.*, 2017, **117**, 2517.

34 I. Osica, G. Imamura, K. Shiba, Q. Ji, L. K. Shrestha, J. P. Hill, K. J. Kurzydłowski, G. Yoshikawa and K. Ariga, Highly Networked Capsular Silica–Porphyrin Hybrid Nanostructures as Efficient Materials for Acetone Vapor Sensing, *ACS Appl. Mater. Interfaces,* 2017, **9**, 9945.

35 D. Wu, A. C. Sedgwick, T. Gunnlaugsson, E. U. Akkaya, J. Yoon and T. D. James, Fluorescent Chemosensors: the Past, Present and Future, *Chem. Soc. Rev.*, 2017, **46**, 7105.

36 V. Ruzsányi, M. P. Kalapos, Breath acetone as a potential marker in clinical practice, *J. Breath Res.* 2017, **11**, 024002.